Enhanced gas sensing response for 2D α-MoO_3 layers: thickness-dependent changes in defect concentration, surface oxygen adsorption, and metal-metal oxide contact

Prashant Bisht[1], Arvind Kumar[1], Ingvild Thue Jensen[2], Mujeeb Ahmad[1], Branson D Belle[2], B.R Mehta[1*]

[1]*Thin Film Laboratory, Department of Physics, Indian Institute of Technology Delhi, New Delhi, 110016, India*

[2] *SINTEF INDUSTRY, Materials Physics, Forskningsveien 1, NO - 0373 Oslo, Norway*

**Corresponding author: brmehta@physics.iitd.ac.in*

Abstract

In this study, α-MoO_3 two-dimensional (2D) layers and thin films were synthesized using pulsed laser deposition technique. X-ray diffraction and Raman spectroscopy confirm the formation of anisotropic α-MoO_3. Atomic Force Microscopy images show the evolution of morphology from 2D layers to oriented crystallite growth with increase in film thickness. Temperature and gas concentration dependent, gas sensing response has been observed to be quite different in 2D layers in comparison to thin film sample. 2D α-MoO_3 layers (~ 6 nm) show higher response of about 25% at a lower temperature (100 °C); They exhibit lower detection limits (up to 100 ppb) and selectivity towards NO_2 gas. Also, 2D layers show p-type gas sensing response and nonlinear current-voltage (I-V) characteristics of metal- metal oxide junctions, in complete contrast to thin film sample, which shows an n-type gas sensing response and linear I-V characteristics. The results have been explained on the basis of lower oxygen defect concentration, enhanced oxygen adsorption at the surface, and metal- α-MoO_3 contact favoring hole conduction.

Keywords: α-MoO_3; Pulsed laser deposition; NO_2; Oxygen vacancies; p-type gas sensing

1. Introduction

Air pollution is one of the major challenges of the 21st century due to the rapid growth of industries and automobiles, causing high emission of air pollutants [1]. There is an ever-increasing need to design and fabricate sensor devices having high response and selectivity along with low fabrication cost and flexible mechanical nature. The two-dimensional materials like graphene and transition metal dichalcogenides (TMDCs) have been extensively explored for miniaturized sensor and actuator applications owing to their unique thickness-dependent physio-chemical properties. In particular, high surface to volume ratio, enhanced surface activity, and fast carrier transport make them suitable for modern gas sensors [2,3].

Two-dimensional transition metal oxides have received less attention as compared to graphene and TMDCs. α-MoO_3 is a two-dimensional (2D) transition metal oxide having atomically thin double layers of thickness 1.4 nm, consisting of a linked distorted MoO_6 octahedra structure. These double layers stack up along the c-axis via weak van der Waals (vdW) forces, where interaction between the atoms within the double-layers is dominated by strong covalent bonding [4,5]. α-MoO_3 is an n-type semiconductor with a wide bandgap of around 3.2 eV to 3.4 eV and a high dielectric constant (6-18). α-MoO_3 has been extensively used for its photochromic [6] and electrochromic [7] properties. It has also been proposed as a candidate for catalysis, gas sensors [8,9], batteries [10], photoelectrochemical cells [11], and solar cells [12]. α-MoO_3 has been obtained previously in many morphologies (like flake,

nanorod, sheet, belt, nanosphere, etc.), using various synthesis techniques like thermal evaporation [13], sputtering [9], pulsed laser deposition (PLD) [14], chemical vapor deposition (CVD) [15], atomic layer deposition (ALD) [16], molecular beam epitaxy (MBE) [17], hydrothermal [8], sol-gel [18], etc. Its structural, electrical, and chemical properties depend upon the synthesis technique employed and corresponding parameters used. Chemo resistive gas sensors based on α-MoO_3 have been demonstrated to be sensitive towards various gases, such as, NO_2, CO, H_2S, H_2 and NH_3 , at elevated temperatures, with detection limits often in ppm range [13,19–22]. However, environmental gas sensing requires lower detection limits, improved selectivity, stability, and energy efficient gas sensors. Response times of a few minutes can be acceptable as environmental conditions change slowly over time.

In this study, we have optimized the growth of α-MoO_3 two-dimensional (2D) layers and thin film using PLD technique. We have studied the thickness-dependent evolution of structural, morphological, and chemical properties of the as-grown films and their gas sensing behavior towards NO_2 gas is discussed in detail. A change from n-type to p-type gas sensing response was observed with decreasing thickness of the α-MoO_3 films. This work may provide a new insight for fabricating the gas sensors based on two-dimensional α-MoO_3 layers to detect a trace amount of NO_2 gas at low operating temperature.

2. Experimental section

2.1. Material synthesis

A molybdenum oxide (MoO_3) PLD target was prepared by grinding MoO_3 powder for 24 hours with 10 ml of 5 % W/V PVA followed by pressing in a uniaxial press and finally sintering the pellet in a muffle furnace for 12 h at 600 °C. A SiO_2/Si substrate of dimension 1.5×1.5 cm^2 was fixed at a distance of 5 cm from the MoO_3 target. The base pressure in the deposition chamber was $4x10^{-6}$ mbar. During the deposition, 30 sccm of O_2 (99.9 %) was introduced into the chamber with deposition pressure maintained at 5.3×10^{-2} mbar, and the substrate temperature was kept at 450 °C. A pulsed KrF excimer laser source (Coherent: Compex 201F) operating at 248 nm and maintained at a 20 ns pulse width with a repetition rate of 5 Hz was used. The laser energy was kept at 75 mJ per pulse, and thin films of α-MoO_3 with thicknesses 70 nm, 18 nm, and 6 nm were synthesized corresponding to 3000, 750 and 250 laser pulses, respectively. Hereafter, the α-MoO_3 thin films having thicknesses 70 nm, 18 nm, and 6 nm are termed as TF (Thin film), UT (Ultrathin film), and 2D (two-dimensional film) respectively.

2.2. Material characterization

The crystallographic structures of all the samples were characterized by X-ray diffraction (XRD) (Rigaku D/max2600 diffractometer) with Cu Kα radiation at wavelength 1.5418 Å. Micro Raman spectroscopy (Renishaw In-Via Raman spectroscope) was used to identify the phase and structure of the as-grown MoO_3 samples. Morphological and microstructural characterizations were performed via field-emission scanning electron microscopy (FESEM) (Jeol: JSM-7800F prime) and atomic force microscope (AFM) (Bruker: Dimension Icon). Surface characterization was done using Kelvin probe force microscopy (KPFM), X-ray photoelectron spectroscopy (XPS) (Kratos Axis $Ultra^{DLD}$ instruments working with

monochromatic Al-kα line, hν = 1486.6 eV) and near ambient pressure XPS (NAP-XPS) (ESCA microscopy beamline, Elettra laboratory).

2.3. Gas sensing measurements

The gas sensing measurement setup as described in Fig. 1 consists of a 700 mL stainless steel chamber with an inbuilt PID controlled heater of area 2.5×2.5 cm^2. The small size of the heater and constant flow of air helps to maintain the chamber temperature near to room temperature during the measurements. It uses a gas mixing setup Serinus Cal 1000 (Ecotec) to achieve the desired concentration of analyte gas. The electrical measurements were performed using a source meter (Keithley 2400) and an in house developed LabVIEW program allowing automatic data acquisition via GPIB interface. Humidity measurements were done by mixing the analyte gas with the humidified air prepared using a bubbler and the percentage relative humidity (% RH) was measured by a standard hygrometer (HTC Instruments HD-304). The sensing device was fabricated using shadow mask deposition of interdigitated electrodes of Ni/Au (20 nm/100 nm) by thermal evaporation on α-MoO_3 samples, as shown in Fig. 1. Gas sensing properties of the devices were determined by measuring the change in the electrical resistance of the sensor in a repeatedly changing gas environment between dry air and target gases like NO_2, NH_3, and CO, at different concentrations and temperatures with a net gas flow rate of 0.56 slpm and relative humidity maintained at 20 % RH for all the measurements. The gas sensor's response (R) is defined as $R = \frac{|Rg - Ra|}{Ra} \times 100$ % where R_a and R_g were the resistance of the sensor in dry air and target gas mixed with the dry air, respectively. The response time is defined as the time required to reach 90 % of the saturation resistance in presence of analyte gas, and the recovery time is the time required to reach 10 % of the saturation resistance value upon

removal of the analyte gas. Initially, the working temperature was determined for each device by measuring the sensing response at different temperatures for 10 ppm NO_2. To reach steady state conditions each sample was stabilized for two hours at a given temperature in dry air before measurements. Subsequently, the sensing response was measured at a fixed operating temperature (~ 100 °C) against different concentrations of NO_2 gas from 100 ppb to 20 ppm.

3. Results and discussion

3.1. Structural and Morphological analysis

In PLD technique, the interaction of intense laser light with solid-state material results in enhanced energy of the adatoms creating a controlled environment for growing crystalline layers along with congruent growth for stoichiometric composition. This makes laser ablation a superior technique as compared to CVD and other PVD (physical vapor deposition) processes [23]. XRD results as shown in Fig. 2(a) indicates three main high-intensity diffraction peaks at 2θ values of 12.69°, 25.72°, 39.04° for 2D, 12.68°, 25.68°, 38.98° for UT and 12.55°, 25.51°, 38.94° for TF samples, and all reflections correspond to (020), (040), and (060) planes of the orthorhombic structure of α phase of MoO_3 (ICDD No 05–0508) [24]. The presence of only (0 k 0) peaks indicates a strongly oriented growth of crystallites in a preferential direction, indicating a layered structure of α-MoO_3. There is a shift in the XRD peaks towards lower 2θ values as the thickness of the film increases. These reflections correspond to the c-lattice plane, which implies an increase in the c-lattice parameter with increasing thickness, which is attributed to the widening of the vdW gap. The widening of the vdW gap due to an increased presence of oxygen vacancies has been reported earlier [25,26]. The c-lattice cell parameter, calculated from the (020) reflections, expands

from 13.93 Å for 2D to 13.94 Å for UT and 14.08 Å for TF sample. The thickness of the sample TF was determined by cross-sectional SEM technique, whereas, for UT, cross-sectional SEM and X-ray reflectivity (XRR) were used, and finally XRR was employed for the 2D sample. The appropriate sample nomenclature has been used based on the results of these techniques.

Raman spectra corresponding to different samples is depicted in Fig. 2(b), and the results show typical peaks of α-MoO_3 at 994, 820, 665, 337, 289, 242, 156, and 124 cm^{-1}. The observed peaks have been assigned to different vibrational modes of α-MoO_3 as per reported literature: 994 cm^{-1} (stretching vibration of Mo bond with terminal oxygen Mo−O along the c-axis), 820 cm^{-1} (stretching in-plane vibration of the Mo−O−Mo with doubly coordinated corner shared oxygen along b-axis), 665 cm^{-1} (Mo−O−Mo stretching with triply coordinated edge shared oxygen), 337 cm^{-1} (O−Mo−O bending mode), 289 cm^{-1} (O=Mo=O wagging mode), 242 cm^{-1} (O=Mo=O twist mode), 156 cm^{-1} (translation vibration of the rigid chains along the a-axis), and 124 cm^{-1} (translation rigid MoO_4 chain mode for the orthorhombic phase of MoO_3) [24,27]. The peak at 820 cm^{-1} corresponds to the layered alpha MoO_3 phase. As the thickness of the sample decreases, the peak intensity also decreases.

AFM images, as shown in Fig. 3 reveal the topography of the as-deposited samples 2D, UT, and TF. Sample 2D consists of a uniform film having two-dimensional domains. Sample UT has a needle-like morphology, the lateral dimensions of needle-like flakes are about 800 nm to 1.2 μm. As the thickness of the film increases with deposition time, the morphology changes from two-dimensional domain to merging needle-like crystallite structure, eventually forming larger crystallites, this is also evident in the FESEM image of the sample TF (Fig. 4). As mentioned earlier that XRD results for the three samples show highly

oriented and preferential growth of crystallites, thus AFM results depict only the evolution of 2D grain growth with increase in the film thickness while preserving the orientation. As shown in Fig. 5(a), the corresponding KPFM images were recorded at room temperature to study the change in the surface potential corresponding to all three samples. It is evident from the surface potential histograms shown in Fig. 5(b) that average surface potential values are -131meV, -44 meV and +34 meV for samples 2D, UT, and TF respectively [28]. These results reveal a large change in the surface potential and the corresponding work function values from 4.62 eV in sample TF to 4.45 eV in sample 2D. This change in the work function can affect the electronic properties of α-MoO_3 with decrease in thickness. It may also play a significant role in determining the nature of electrical contacts formed with the α-MoO_3 thin film.

3.2. XPS analysis

XPS spectra of Mo 3d, valence band maxima, and O 1s peaks of sample 2D and TF were studied to determine the chemical composition and valence state of the samples. High resolution spectra were collected at pass energy of 40 eV and a step size of 0.05 eV for both core level peaks and valence band (VB) maxima region. The C 1s peak of adventitious carbon (284.8 eV) was used to calibrate the energy axis. As shown in Fig. 6(a, b), Mo 3d doublet peak of sample 2D and TF was deconvoluted into two peaks corresponding to Mo $3d_{5/2}$ and Mo $3d_{3/2}$ for oxidation states Mo^{6+} and Mo^{5+} [29]. The higher intensity Mo^{6+} peak represents the stoichiometric α-MoO_3, and the lower intensity Mo^{5+} peak represents the lower oxidation state due to the presence of oxygen vacancies [30,31]. There is a minor shift (~ 0.06 eV) in the peaks of Mo $3d_{5/2}$ Mo^{6+} and Mo $3d_{3/2}$ Mo^{6+} components of sample 2D towards higher binding energy (B.E.) as compared to sample TF. Also, the deconvoluted

component Mo $3d_{5/2}$ Mo^{5+} and Mo $3d_{3/2}$ Mo^{5+} of sample 2D has a shift of 0.17 eV and 0.28 eV, respectively, towards higher B.E. as compared to sample TF. These shifts show the presence of higher concentration of oxygen vacancies in TF as compared to 2D. The relative intensities of the Mo^{6+} and Mo^{5+} peaks in both TF and 2D confirm that Mo is present mainly in the +6 oxidation state, this comparison is also shown in Fig. 6(c). A survey spectrum is used to calculate the atomic ratio O/Mo, which is 2.66 for TF and 2.89 for 2D. Sample TF is more off stoichiometric as compared to 2D. The VB maxima spectra of sample 2D and TF, as shown in Fig. 6(d), shows the defect states present within the band gap and the valence band edge is located at 3.21 eV (for 2D) and 3.28 eV (for TF) below Fermi level.

The O 1s peak corresponding to 2D and TF is shown in Fig. 7. The most intense component of deconvoluted O 1s peak for 2D (530.49 eV) and TF (530.93 eV) is attributed to metal-oxygen (Mo-O) bonds. The shoulder peaks at 532.06 eV and 532.12 eV for 2D and TF respectively corresponds to peroxo groups (O_2^{2-}) connected to the Mo atom related to the adsorbed oxygen [32]. The percentage of the adsorbed oxygen in the sample 2D (37.43%) is high as compared to TF (28.12%), which indicates more reactive sites on the 2D surface as compared to TF due to its two-dimensional nature, and thus, rendering it more reactive with the atmospheric oxygen.

One of the objectives of the present study is to examine the gas sensing behavior with decreasing thickness. Near ambient pressure (NAP) XPS measurements [33] were carried out on sample 2D and TF, using the ESCA microscopy beamline. This technique enables one to study the chemical composition and valence state of the sample in the presence of target gases at the desired working temperature.

The above mentioned XPS studies were carried out on sample 2D and TF, first in vacuum and then in the presence of a 50:50 mixture of NO_2 and NO gas diluted in argon at a pressure of about ~ 10^{-2} mbar in the NAP cell. High resolution spectra were collected at pass energy of 20 eV and a step size of 0.08 eV for both core peaks and VB maxima region. Here also the C 1s peak of adventitious carbon (284.8 eV) was used to calibrate the energy axis. A focused X-ray beam of spot size 75 μm^2 was incident on the sample surface, and the XPS spectra corresponding to Mo 3d peak was recorded. The samples 2D and TF were maintained at a temperature of 156 °C and 250 °C respectively, for maximum surface reaction with NO_2 and NO gas mixture. As will be shown later in the sensing results, these samples exhibit higher sensing response at these temperatures. Fig. 8(a, b) shows the deconvoluted Mo 3d peaks for sample 2D in vacuum and gas mixture, respectively. The relative intensity of the deconvoluted Mo 3d peaks in 2D confirms that Mo is present predominantly in the +5 oxidation state with minority content in +6 and +4 oxidation states. However, the spectrum recorded with sample in the gas mixture reveals peak shifts towards higher B.E. (as shown in Fig. 8(c) and stated in Table 1) with an increase in the relative intensity of the +6 oxidation state, as compared to peaks observed with sample kept in a vacuum environment. For sample TF, a similar result was observed with the sample in vacuum environment inside NAP cell, exhibiting +5 as the dominant oxidation state. It is interesting to note that no change was observed on the introduction of the gas mixture in the case of TF, as shown in Fig. 8(d). The shift towards higher B.E. and change in the relative intensity indicates the reaction of the sensing gas with α-MoO_3 surface, resulting in higher oxidation of the 2D sample surface, unlike sample TF. Also, as shown in Fig. 8(e, f), the VB maxima spectra of sample 2D indicate a decrease in the concentration of defect states within the bandgap in the presence

of gas mixture, which is related to its high surface reactivity. However, no significant change in the VB maxima spectra of sample TF was observed on the introduction of gas mixture. The observed dominance of the +5 oxidation state in NAP XPS results in comparison to the domination of the +6 oxidation state in regular UHV XPS results may be because of damage caused by the focused X-ray beam from the synchrotron. The sample spot exposed to X-ray was continuously changed to reduce the effect mentioned above.

3.3. Gas sensing analysis

Gas sensing properties of sample 2D, UT, and TF towards NO_2 gas were studied in detail. The working temperature was optimized using the sensing response of samples 2D, UT, and TF towards 10 ppm of NO_2 gas with sample temperatures ranging from room temperature (RT) to 250 °C. The results shown in Fig. 9(a) depicts a volcanic shaped curve of sensing response vs temperature behavior for samples 2D and UT. At lower operating temperatures, there is low energy to cross the activation energy barrier, slow surface reactions between adsorbed gas molecules and sensor surface which results in lower response. On increasing the temperature, the plot peaks to a maximum sensing response of 25 % for 2D and 15 % for UT at an operating temperature of 100 °C and 150 °C, respectively which may be due to an increase in thermal energy which causes an increase in surface reactions and higher rate of adsorption leading to a maximum sensor response. On further increase of temperature the adsorption rate is reduced, and target gas molecules escape from the film surface before reaction takes place, resulting in a decline in the sensor response [34,35]. Moreover, the decreased response in 2D and UT may also be attributed to the rise in the electron concentration resulting from the thermal excitation of electrons from the VB, thereby reducing the p-type behavior, hence a decreased response at higher temperatures. Whereas

the sensing response of sample TF increases linearly from RT to 250 °C (up to 35 %). This may be attributed to the enhanced surface adsorption of NO_2 and oxygen species owing to faster surface kinetics. A comparison of sensing response at 100 °C reveals the highest value for sample 2D, and the sensing response declines as one goes to UT and then to sample TF. The lower optimum operating temperature with the decreasing thickness of α-MoO_3 depicts a change in the sensing response with thickness owing to the change in the electronic properties, as discussed earlier.

The lowest detection limit towards NO_2 was determined by measuring the response at different concentrations of NO_2 gas in the range of 100 ppb to 20 ppm, at 100 °C temperature, which is displayed in Fig. 9(b, c). The minimum detection limit towards NO_2 for sample TF was 5 ppm, it gradually decreases with the thickness of the film and it is observed to be 500 ppb for UT and 100 ppb for the sample 2D. The large surface to volume ratio in 2D due to lower thickness provides larger number of active sites, which enables high oxygen and NO_2 adsorption resulting in low detection limit at low operating temperature. This phenomenon is also evident in many other two-dimensional materials having limit of detection of few ppb at low working temperatures[36].

Fig. 9(d)-(f) depicts the dynamic response curve. This shows the resistance vs. time plot for a given sample in terms of repeated response and recovery cycles at their corresponding optimized working temperature towards 10 ppm of NO_2 gas. The results show typical n-type gas sensing behavior for sample TF but p-type gas sensing behavior for samples 2D and UT. Also, inset of Fig. 9 (d) and (e) exhibits a consistent p-type behavior even at higher operating temperature of 200 °C for 10 ppm NO_2 gas. The p-type sensing behavior in sample 2D and UT can be attributed to the strong surface adsorption of the oxygen species, which results in

a depletion or an inversion layer at the surface of the film. This effect is further enhanced due to the adsorption of NO_2 during gas sensing measurements. In addition, the role of metal-metal oxide contact may be another factor in this behavior, as will be discussed later.

To check the selectivity of proposed sensors, the sensing response of 2D and TF was also measured towards other potentially hazardous gases like NH_3 and CO. Sensing towards 100 ppm NH_3 gas show response value of 4.5 % for sample 2D operating at 100 °C and 3 % for sample TF operating at 200 °C. In the case of 100 ppm CO, it was observed to be within the measurement noise limit for both 2D and TF. This may be attributed to different reaction kinematics of sensor device towards different analyte gas molecules. It confirms that the sensor is selective towards NO_2 gas. Here also, TF shows a usual n-type gas sensing behavior, whereas 2D shows p-type gas sensing behavior corresponding to NH_3 and CO gases.

Response and recovery time are the two important parameters of a gas sensor. Table 2 compares the response and recovery time of sample 2D, UT and TF for 10 ppm NO_2 at 100 °C and 200 °C. The response time in 2D at 100 °C was 200 s with an incomplete recovery, which is lowest as compared to UT and TF. This may be attributed to the depletion region created in sample 2D due to the strong adsorption of oxygen species (O^- and O_2^-) which may extend to larger portion of the film thickness as compared to UT and TF. Therefore, any change in the conductivity of the film will be highly sensitive to the adsorbed NO_2 molecules resulting in faster and higher sensing response, thereby shorter response time. On further increase in temperature to 175 °C, sample 2D shows a shorter response time of 123 s and full recovery owing to high thermal energy for the desorption of NO_2 molecules from the film surface. Also, the response and recovery cycle at 200 °C as shown in inset of Fig. 9 (d)-

(f) depicts complete response and recovery at higher temperature for all three samples. Table S1 depicts sample 2D shows good response, low detection limits, and relatively shorter response time at low operating temperatures when compared to other similar studies on MoO_3 and other nanostructured materials, respectively.

The effect of humidity on sample 2D and TF at two different RH values, namely, 20 % and 85 % has been investigated to study the response at a working temperature of 100 °C when exposed to 10 ppm NO_2. As concluded from the measurements performed, a change in the baseline resistance from 112 kΩ to 136 kΩ was observed. This increase in resistance is due the adsorption of water (H_2O) molecules which may dissociate to give hydroxyl group (OH^-) at this working temperature and they can donates electrons according to the Heiland and Kohl mechanism [37,38], thus, reducing the p-type conductivity. Decrease in sensing response from 20 % to 16 % was also observed and the reason might be attributed to the decreased number of active sites due to adsorption of the H_2O molecules and hydroxyl (OH^-) group resulting in limited adsorption of oxygen and NO_2 species. In sample TF a decrease in the baseline resistance from 40.2 kΩ to 38.46 kΩ was observed due to the donation of electron by the adsorbed hydroxyl group (OH^-) and a small change in sensing response from 6 % to 5.3 % was observed. In both low and high humidity values samples 2D and TF shows p and n- type sensing behavior, respectively. This confirms that there is no effect of humidity on the change in n-type to p-type gas sensing behavior on going from sample TF to 2D.

3.4. Mechanism of gas sensing

The sensing mechanism of chemo resistive gas sensors is based upon the change in electrical conductivity (carrier concentration) of the sensing material on reaction with the target gas molecules. Oxide semiconductors adsorb oxygen from the ambient environment and form

oxygen species like O^-, O^{2-} and O_2^- at the semiconductor surface via following chemical reactions:

$O_2\,(gas) + e^- \rightarrow O_2^-\,(ads)$ stable for temperature < 100 °C (1)

$O_2^-\,(ads) + e^- \rightarrow 2O^-\,(ads)$ stable for temperature between 100 °C to 300 °C (2)

$O^-\,(ads) + e^- \rightarrow O^{2-}\,(ads)$ stable for temperature > 300 °C (3)

These chemical reactions indicate that the electrons are consumed from the conduction band, forming a surface depletion layer resulting in a decrease in the conductivity of n-type semiconductor (increase in case of p-type semiconductor).

NO_2 is oxidizing in nature and it can react directly with the oxide surface or indirectly via adsorbed oxygen species already present on the surface via the following chemical reactions [22]:

$NO_2\,(gas) + e^- \rightarrow NO_2^-\,(ads)$ (4)

$NO_2\,(gas) + O^-\,(ads) + 2e^- \rightarrow NO_2^-\,(ads) + O^{2-}\,(ads)$ (5)

$NO_2\,(gas) + 2e^- + O_2^-\,(gas) \rightarrow NO_2^-\,(ads) + 2O^-\,(ads)$ (6)

Electron affinity of NO_2 (2.273 eV) [39] is higher than that of O_2 (0.450 eV) [40]; therefore, NO_2 may take more electrons from the surface. In both cases, electrons are lost from the surface, hence the conductivity decreases for n-type (increases for p-type) semiconductor. In case of reducing gases like CO and NH_3, which donate electrons to the surface, the conductivity increases for n-type (decreases for p-type) semiconductor.

α-MoO_3, in its stoichiometric form, is an insulator. However, it is mostly found as an n-type semiconductor due to the formation of oxygen vacancies. Control over the oxygen

vacancies in α-MoO_3 has been used earlier to tune its electronic and chemical properties [41–43]. A typical oxygen vacancy formation process may be represented in terms of the following reaction:

$$O_0 \leftrightarrow \frac{1}{2} O_2\,(gas) + V_O^{\cdot\cdot} + 2e' \quad (7)$$

where O_0 represents an unstable oxygen atom in an oxygen site and $V_O^{\cdot\cdot}$ represents the oxygen vacancy with a double positive charge. When these oxygen vacancies are filled with oxygen during annealing in the air or during sensing the following reaction takes place:

$$V_O^{\cdot\cdot} + \frac{1}{2} O_2\,(gas) \leftrightarrow O_0 + 2h^{\cdot} \quad (8)$$

This reaction results in a decrease in the electron concentration due to high oxygen adsorption [18,44]. It is observed in earlier reports [45] that due to enhanced surface adsorption of oxygen species, a surface inversion layer may be formed, resulting in conductivity dictated by hole concentration in the surface layer.

It is evident from the deconvoluted Mo 3d peaks of the XPS spectra that sample 2D has a lower concentration of free electrons due to lower oxygen vacancies as compared to sample TF. Also, O 1s peak of sample 2D show higher oxygen adsorption due to its high surface to volume ratio as compared to TF. The high surface reactivity of sample 2D as compared to TF is confirmed from their respective ambient pressure XPS measurements. As the thickness of the sample 2D is lower, it can be inferred that the carriers will be depleted from the complete thickness of the sample 2D and may form surface inversion layer.

It is also important to compare the results of I-V measurements of sample 2D, UT, and TF, as shown in Fig. 10 to understand the metal- α-MoO_3 contact. Sample TF shows an ohmic

behavior with lower resistance as compared to non-ohmic behavior observed in sample 2D and UT. This indicates a transformative change in the electronic properties of the oxide layer with a decrease in the film thickness. Hence on moving from sample TF to 2D, the deviation from linear I-V characteristic seems to increase. This nonlinear behavior in 2D and UT can be attributed to a considerable level of Schottky barrier at metal- α-MoO_3 contact, which can modulate the type of charge carrier inside the conductive channel by creating a barrier for electrons and allowing holes to pass. As deduced from the KPFM measurements there is a decrease in work function values from sample TF to 2D. Further sample 2D is less n-type as compared to TF due to lower oxygen vacancies suggesting that the Fermi level is nearer to the conduction band in sample TF as compared to 2D. This indicates a larger difference in the work function of metal and electron affinity of sample 2D and UT, which may result in a higher Schottky barrier height as compared to sample TF and also a higher Schottky barrier width which may result from the depletion of the entire 2D film thickness under the contact region, as shown in Fig. 11(a). As the thickness of 2D sample is less as compared to the expected depletion layer thickness, accumulation of excess charge in the case of sample 2D can also contribute to a higher Schottky barrier [46]. In contrast, for sample TF, this barrier is rather small, and electrons can cross the barrier easily.

Under the applied bias, current transport takes place via holes in sample 2D and UT as they are depleted of electrons in the conducting channel and have high Schottky barrier. The presence of NO_2 further reduces the electron concentration, resulting in an upward shift of the VB, as shown in Fig. 11 (b), thereby increasing the hole current, hence higher p-type sensing response [47]. This is effectual even for low NO_2 concentrations and low temperature due to the large number of surface reactive sites in 2D and UT due to their high

surface to volume ratio. However, sample TF shows n-type gas sensing behavior upon NO_2 gas exposure. This is due to its large electron concentration and low oxygen adsorption (as evident from XPS measurements). This kind of n to p-type change in gas sensing behavior is also observed in metal oxides, such as, SnO_2 [48] , Fe_2O_3 [45], and ZnO [44] under certain conditions. Thus, a fine balance between the surface to volume ratio and the concentration of oxygen vacancies is crucial for the improved gas sensing behavior of α-MoO_3 films.

4. Conclusions

Two dimensional (2D), ultrathin (UT), and thin films (TF) of α-MoO_3 were synthesized using pulsed laser deposition technique. XRD and Raman studies confirm the α-MoO_3 phase with a layered structure in all the samples. AFM images display the evolution of morphology starting from 2D domains, merging to form an ultrathin layer, and finally, a thin film structure all having a preferred direction of growth. XPS studies show higher concentration of oxygen vacancies in sample TF as compared to sample 2D and higher oxygen adsorption in sample 2D as compared to sample TF. Gas sensing behavior and I-V characteristics indicates a transformative change in the electronic nature with sample 2D and UT showing p-type sensing response and nonlinear junction characteristics in comparison to n-type response and ohmic metal- metal oxide junction behavior in sample TF. Sample 2D exhibits selective response towards NO_2 with a minimum detection limit of 100 ppb and the highest response value of 25% at 100 °C. The dependence of sensing response on temperature is quite different in sample 2D with response peaking at 100 °C in comparison to sample TF, in which it gradually increases from RT to 250 °C. The effect of humidity was more evident on sample 2D as compared to TF. The results have been explained on the basis of lower

oxygen vacancy concentration, higher oxygen adsorption due to the high surface to volume ratio, and high Schottky barrier at metal-α- MoO_3 junction in sample 2D and UT in comparison to sample TF.

Acknowledgment

The authors are grateful to Dr. Luca Gregoratti, Dr. Matteo Amati, and Dr. Patrick Zeller for their experimental contributions and discussions over ESCA microscopy experiment at Elettra synchrotron. We thank Nanoscale Research Facility (NRF), IIT Delhi, for providing the Raman and XRD facility. Prashant Bisht wishes to thank UGC, India, for providing junior research fellowship. B.R.M. acknowledges the support provided by DST-NANO mission and Schlumberger Chair Professorship

Funding: This work is supported by the Department of Science and Technology, India (Project no. DST/INT/NOR/RCN/ICT/P-04/2018) and The Research Council of Norway (Project no. 250555).

References

[1] M. Ammann, M. Kalberer, D.T. Jost, L. Tobler, E. Rössler, D. Piguet, H.W. Gäggeler, U. Baltensperger, Heterogeneous production of nitrous acid on soot in polluted air masses, Nature. 395 (1998) 157–160. https://doi.org/10.1038/25965.

[2] W. Fu, L. Jiang, E.P. van Geest, L.M.C. Lima, G.F. Schneider, Sensing at the Surface of Graphene Field-Effect Transistors, Adv. Mater. 29 (2017) 1603610. https://doi.org/10.1002/adma.201603610.

[3] X. Liu, T. Ma, N. Pinna, J. Zhang, Two-Dimensional Nanostructured Materials for Gas Sensing, Adv. Funct. Mater. 27 (2017) 1702168. https://doi.org/10.1002/adfm.201702168.

[4] S. Guimond, D. Göbke, J.M. Sturm, Y. Romanyshyn, H. Kuhlenbeck, M. Cavalleri, H.-J. Freund, Well-Ordered Molybdenum Oxide Layers on Au(111): Preparation and Properties, J. Phys. Chem. C. 117 (2013) 8746–8757. https://doi.org/10.1021/jp3113792.

[5] D. Wang, J.N. Li, Y. Zhou, D.H. Xu, X. Xiong, R.W. Peng, M. Wang, Van der Waals epitaxy of ultrathin α-MoO_3 sheets on mica substrate with single-unit-cell thickness, Appl. Phys. Lett. 108 (2016) 1–6. https://doi.org/10.1063/1.4941402.

[6] J.N. Yao, K. Hashimoto, A. Fujishima, Photochromism induced in an electrolytically pretreated MoO_3 thin film by visible light, Nature. 355 (1992) 624–626. https://doi.org/10.1038/355624a0.

[7] A. Guerfi, Characterization and Stability of Electrochromic MoO_3 Thin Films Prepared by Electrodeposition, J. Electrochem. Soc. 142 (1995) 3457. https://doi.org/10.1149/1.2050004.

[8] Y. Mo, Z. Tan, L. Sun, Y. Lu, X. Liu, Ethanol-sensing properties of α-MoO_3 nanobelts synthesized by hydrothermal method, J. Alloys Compd. 812 (2020) 152166. https://doi.org/10.1016/j.jallcom.2019.152166.

[9] M. Ferroni, V. Guidi, G. Martinelli, P. Nelli, M. Sacerdoti, G. Sberveglieri, Characterization of a molybdenum oxide sputtered thin film as a gas sensor, Thin Solid Films. 307 (1997) 148–151. https://doi.org/10.1016/S0040-6090(97)00279-4.

[10] S.-H. Lee, Y.-H. Kim, R. Deshpande, P.A. Parilla, E. Whitney, D.T. Gillaspie, K.M. Jones, A.H. Mahan, S. Zhang, A.C. Dillon, Reversible Lithium-Ion Insertion in Molybdenum Oxide Nanoparticles, Adv. Mater. 20 (2008) 3627–3632. https://doi.org/10.1002/adma.200800999.

[11] N. Kodan, A.P. Singh, M. Vandichel, B. Wickman, B.R. Mehta, Favourable band edge alignment and increased visible light absorption in β-MoO_3/α-MoO_3 oxide heterojunction for enhanced photoelectrochemical performance, Int. J. Hydrogen Energy. 43 (2018) 15773–15783. https://doi.org/10.1016/j.ijhydene.2018.06.138.

[12] N. Chaturvedi, S.K. Swami, V. Dutta, Electric field assisted spray deposited MoO_3 thin films as a hole transport layer for organic solar cells, Sol. Energy. 137 (2016) 379–384. https://doi.org/10.1016/j.solener.2016.08.038.

[13] M.B. Rahmani, S.H. Keshmiri, J. Yu, A.Z. Sadek, L. Al-Mashat, A. Moafi, K. Latham, Y.X. Li, W. Wlodarski, K. Kalantar-zadeh, Gas sensing properties of thermally evaporated lamellar MoO_3, Sensors Actuators B Chem. 145 (2010) 13–19. https://doi.org/10.1016/j.snb.2009.11.007.

[14] S.S. Sunu, E. Prabhu, V. Jayaraman, K.I. Gnanasekar, T. Gnanasekaran, Gas sensing properties of PLD made MoO_3 films, Sensors Actuators B Chem. 94 (2003) 189–196.

https://doi.org/10.1016/S0925-4005(03)00342-3.

[15] K. Gesheva, A. Szekeres, T. Ivanova, Optical properties of chemical vapor deposited thin films of molybdenum and tungsten based metal oxides, Sol. Energy Mater. Sol. Cells. 76 (2003) 563–576. https://doi.org/10.1016/S0927-0248(02)00267-2.

[16] Z. Wei, Z. Hai, M.K. Akbari, D. Qi, K. Xing, Q. Zhao, F. Verpoort, J. Hu, L. Hyde, S. Zhuiykov, Atomic layer deposition-developed two-dimensional α-MoO_3 windows excellent hydrogen peroxide electrochemical sensing capabilities, Sensors Actuators B Chem. 262 (2018) 334–344. https://doi.org/10.1016/j.snb.2018.01.243.

[17] K. Koike, R. Wada, S. Yagi, Y. Harada, S. Sasa, M. Yano, Characteristics of MoO_3 films grown by molecular beam epitaxy, Jpn. J. Appl. Phys. 53 (2014) 05FJ02. https://doi.org/10.7567/jjap.53.05fj02.

[18] A.K. Prasad, D.J. Kubinski, P.I. Gouma, Comparison of sol–gel and ion beam deposited MoO_3 thin film gas sensors for selective ammonia detection, Sensors Actuators B Chem. 93 (2003) 25–30. https://doi.org/10.1016/S0925-4005(03)00336-8.

[19] M.M.Y.A. Alsaif, S. Balendhran, M.R. Field, K. Latham, W. Wlodarski, J.Z. Ou, K. Kalantar-zadeh, Two dimensional α-MoO_3 nanoflakes obtained using solvent-assisted grinding and sonication method: Application for H_2 gas sensing, Sensors Actuators B Chem. 192 (2014) 196–204. https://doi.org/10.1016/j.snb.2013.10.107.

[20] A.T. Güntner, M. Righettoni, S.E. Pratsinis, Selective sensing of NH_3 by Si-doped α-MoO_3 for breath analysis, Sensors Actuators B Chem. 223 (2016) 266–273. https://doi.org/10.1016/j.snb.2015.09.094.

[21] H.M.M. Munasinghe Arachchige, D. Zappa, N. Poli, N. Gunawardhana, E. Comini, Gold functionalized MoO_3 nano flakes for gas sensing applications, Sensors Actuators B Chem. 269 (2018) 331–339. https://doi.org/10.1016/j.snb.2018.04.124.

[22] A.A. Mane, M.P. Suryawanshi, J.H. Kim, A. V Moholkar, Highly selective and sensitive response of 30.5 % of sprayed molybdenum trioxide (MoO_3) nanobelts for nitrogen dioxide (NO_2) gas detection, J. Colloid Interface Sci. 483 (2016) 220–231. https://doi.org/10.1016/j.jcis.2016.08.031.

[23] G.K.H. D.B. Chrisey, Pulsed Laser Deposition, John Wiley, New York, n.d.

[24] S. Dayal, C.S. Kumar, Development of hierarchical layered nanostructured α-MoO_3 thin films using dc magnetron sputtering, Mater. Res. Express. 3 (2016) 106405. https://doi.org/10.1088/2053-1591/3/10/106405.

[25] H.-S. Kim, J.B. Cook, H. Lin, J.S. Ko, S.H. Tolbert, V. Ozolins, B. Dunn, Oxygen vacancies enhance pseudocapacitive charge storage properties of MoO_{3-x}, Nat. Mater. 16 (2017) 454–460. https://doi.org/10.1038/nmat4810.

[26] Q.-L. Wu, S.-X. Zhao, L. Yu, X.-X. Zheng, Y.-F. Wang, L.-Q. Yu, C.-W. Nan, G. Cao, Oxygen vacancy-enriched MoO_{3-x} nanobelts for asymmetric supercapacitors with excellent room/low temperature performance, J. Mater. Chem. A. 7 (2019) 13205–13214. https://doi.org/10.1039/C9TA03471D.

[27] Y. Wang, X. Du, J. Wang, M. Su, X. Wan, H. Meng, W. Xie, J. Xu, P. Liu, Growth of Large-Scale, Large-Size, Few-Layered α-MoO_3 on SiO_2 and Its Photoresponse Mechanism, ACS Appl. Mater. Interfaces. 9 (2017) 5543–5549. https://doi.org/10.1021/acsami.6b13743.

[28] I. Horcas, R. Fernández, J.M. Gómez-Rodríguez, J. Colchero, J. Gómez-Herrero, A.M. Baro,

WSXM: A software for scanning probe microscopy and a tool for nanotechnology, Rev. Sci. Instrum. 78 (2007) 13705. https://doi.org/10.1063/1.2432410.

[29] A.A. Mane, A. V Moholkar, Palladium (Pd) sensitized molybdenum trioxide (MoO_3) nanobelts for nitrogen dioxide (NO_2) gas detection, Solid. State. Electron. 139 (2018) 21–30. https://doi.org/10.1016/j.sse.2017.09.011.

[30] S.S. Sunu, E. Prabhu, V. Jayaraman, K.I. Gnanasekar, T.K. Seshagiri, T. Gnanasekaran, Electrical conductivity and gas sensing properties of $MoO_3$1Dedicated to Prof. Adolf Mikula, University of Vienna on the occasion of his 60th birthday.1, Sensors Actuators B Chem. 101 (2004) 161–174. https://doi.org/10.1016/j.snb.2004.02.048.

[31] S. Bai, S. Chen, L. Chen, K. Zhang, R. Luo, D. Li, C.C. Liu, Ultrasonic synthesis of MoO_3 nanorods and their gas sensing properties, Sensors Actuators B Chem. 174 (2012) 51–58. https://doi.org/10.1016/j.snb.2012.08.015.

[32] A.A. Bortoti, A. de Freitas Gavanski, Y.R. Velazquez, A. Galli, E.G. [de Castro], Facile and low cost oxidative conversion of MoS_2 in α-MoO_3: Synthesis, characterization and application, J. Solid State Chem. 252 (2017) 111–118. https://doi.org/10.1016/j.jssc.2017.05.006.

[33] H. Sezen, M. Al-Hada, M. Amati, L. Gregoratti, In situ chemical and morphological characterization of copper under near ambient reduction and oxidation conditions, Surf. Interface Anal. 50 (2018) 921–926. https://doi.org/10.1002/sia.6276.

[34] S. Bai, C. Chen, D. Zhang, R. Luo, D. Li, A. Chen, C.-C. Liu, Intrinsic characteristic and mechanism in enhancing H_2S sensing of Cd-doped α-MoO_3 nanobelts, Sensors Actuators B Chem. 204 (2014) 754–762. https://doi.org/10.1016/j.snb.2014.08.017.

[35] A. Kumar, A. Sanger, A. Kumar, R. Chandra, Highly sensitive and selective CO gas sensor based on a hydrophobic SnO_2/CuO bilayer, RSC Adv. 6 (2016) 47178–47184. https://doi.org/10.1039/C6RA06538D.

[36] C. Anichini, W. Czepa, D. Pakulski, A. Aliprandi, A. Ciesielski, P. Samorì, Chemical sensing with 2D materials, Chem. Soc. Rev. 47 (2018) 4860–4908. https://doi.org/10.1039/C8CS00417J.

[37] Z. Bai, C. Xie, M. Hu, S. Zhang, D. Zeng, Effect of humidity on the gas sensing property of the tetrapod-shaped ZnO nanopowder sensor, Mater. Sci. Eng. B. 149 (2008) 12–17. https://doi.org/10.1016/j.mseb.2007.11.020.

[38] N. Barsan, U. Weimar, Conduction Model of Metal Oxide Gas Sensors, J. Electroceramics. 7 (2001) 143–167. https://doi.org/10.1023/A:1014405811371.

[39] K.M. Ervin, J. Ho, W.C. Lineberger, Ultraviolet photoelectron spectrum of nitrite anion, J. Phys. Chem. 92 (1988) 5405–5412. https://doi.org/10.1021/j100330a017.

[40] Spin -Orbit Coupling in the O^-_2 Anion , Zeitschrift Für Naturforsch. A . 50 (1995) 1041. https://doi.org/10.1515/zna-1995-1110.

[41] S. Shen, X. Zhang, X. Cheng, Y. Xu, S. Gao, H. Zhao, X. Zhou, L. Huo, Oxygen-Vacancy-Enriched Porous α-MoO_3 Nanosheets for Trimethylamine Sensing, ACS Appl. Nano Mater. 2 (2019) 8016–8026. https://doi.org/10.1021/acsanm.9b02072.

[42] J. Yang, X. Xiao, P. Chen, K. Zhu, K. Cheng, K. Ye, G. Wang, D. Cao, J. Yan, Creating oxygen-vacancies in MoO_{3-x} nanobelts toward high volumetric energy-density asymmetric supercapacitors with long lifespan, Nano Energy. 58 (2019) 455–465. https://doi.org/10.1016/j.nanoen.2019.01.071.

[43] D. Xiang, C. Han, J. Zhang, W. Chen, Gap States Assisted MoO_3 Nanobelt Photodetector with Wide Spectrum Response, Sci. Rep. 4 (2014) 4891. https://doi.org/10.1038/srep04891.

[44] J.X. Wang, X.W. Sun, Y. Yang, C.M.L. Wu, N\P transition sensing behaviors of ZnO nanotubes exposed to NO_2 gas, Nanotechnology. 20 (2009) 465501. https://doi.org/10.1088/0957-4484/20/46/465501.

[45] Y.-C. Lee, Y.-L. Chueh, C.-H. Hsieh, M.-T. Chang, L.-J. Chou, Z.L. Wang, Y.-W. Lan, C.-D. Chen, H. Kurata, S. Isoda, p-Type α-Fe_2O_3 Nanowires and their n-Type Transition in a Reductive Ambient, Small. 3 (2007) 1356–1361. https://doi.org/10.1002/smll.200700004.

[46] M. Ahmad, D. Varandani, B.R. Mehta, Large surface charge accumulation in 2D MoS_2/Sb_2Te_3 junction and its effect on junction properties: KPFM based study, Appl. Phys. Lett. 113 (2018) 141603. https://doi.org/10.1063/1.5042499.

[47] K.Y. Ko, J.-G. Song, Y. Kim, T. Choi, S. Shin, C.W. Lee, K. Lee, J. Koo, H. Lee, J. Kim, T. Lee, J. Park, H. Kim, Improvement of Gas-Sensing Performance of Large-Area Tungsten Disulfide Nanosheets by Surface Functionalization, ACS Nano. 10 (2016) 9287–9296. https://doi.org/10.1021/acsnano.6b03631.

[48] N. Bârsan, R. Grigorovici, R. Ionescu, M. Motronea, A. Vancu, Mechanism of gas detection in polycrystalline thick film SnO_2 sensors, Thin Solid Films. 171 (1989) 53–63. https://doi.org/10.1016/0040-6090(89)90033-3.

Figures:

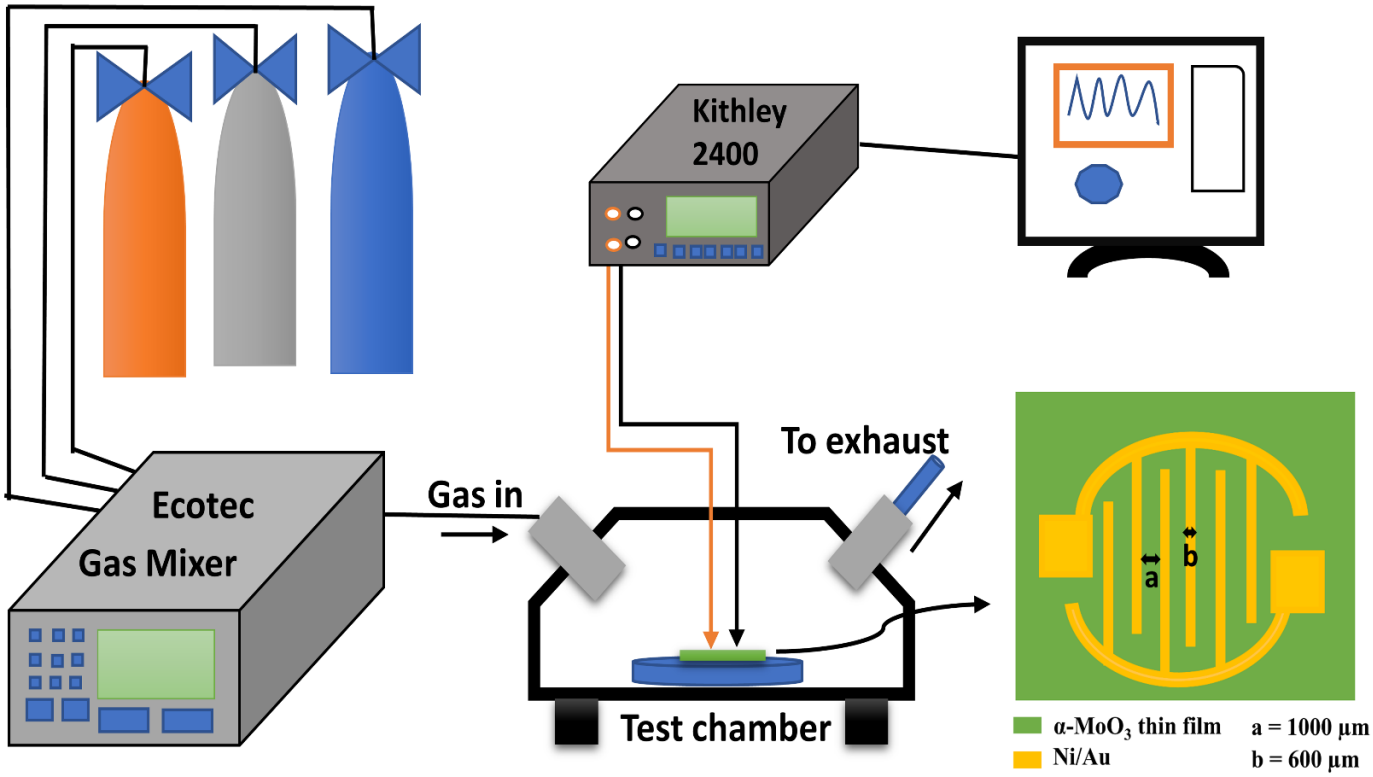

Fig. 1. Schematic diagram of the gas sensing setup and IDE electrode on α-MoO_3 sample.

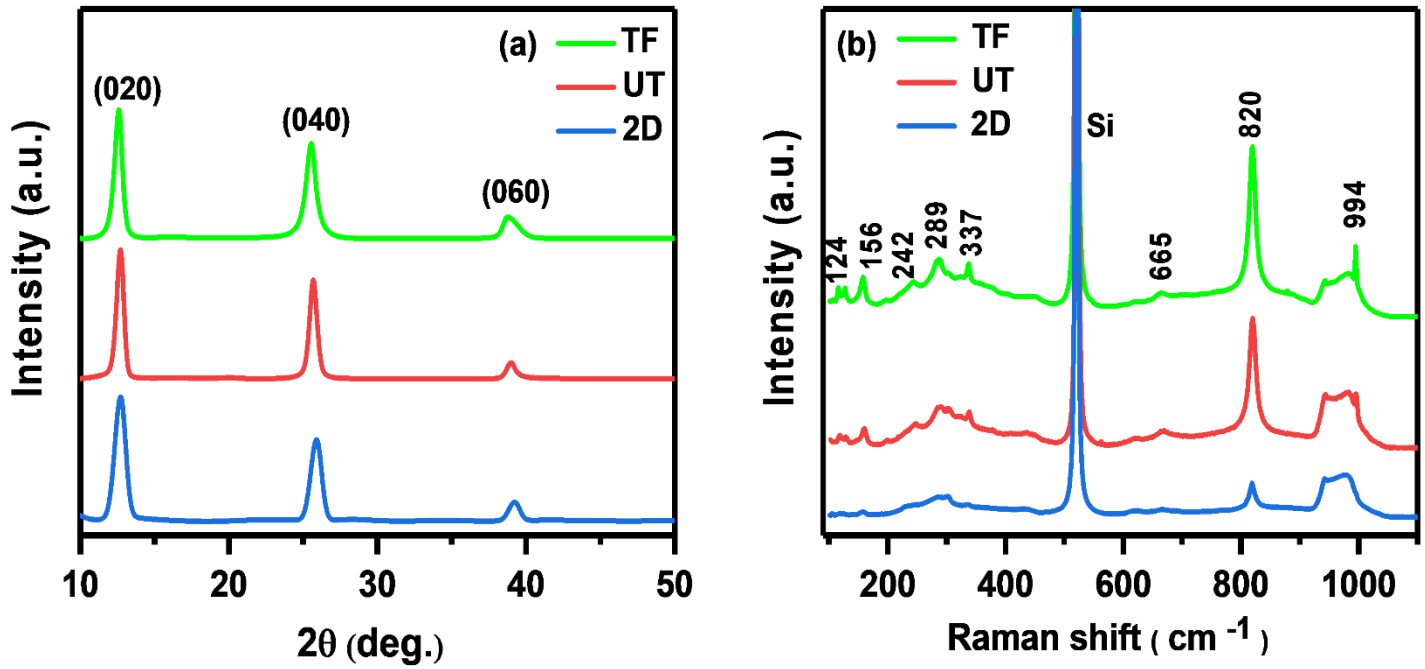

Fig. 2. (a) XRD pattern for sample 2D, UT, and TF. The diffraction intensity for the (020), (040), and (060) peaks indicate preferentially oriented films along the [0k0] direction. (b) Room temperature Raman spectra (excitation wavelength 532 nm) for sample 2D, UT, and TF. Raman spectra peaks indicate the formation of the α- phase of MoO_3.

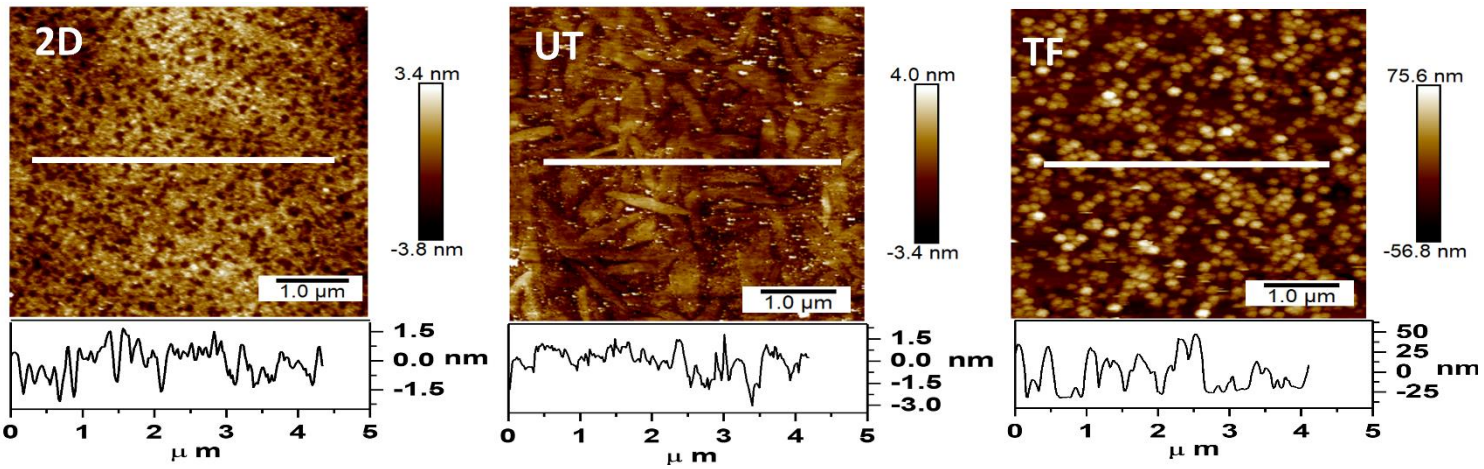

Fig. 3. AFM investigation of the as-deposited α-MoO_3 films. Morphology plots of sample 2D, UT, and TF show the evolution of α-MoO_3 thin film with thickness.

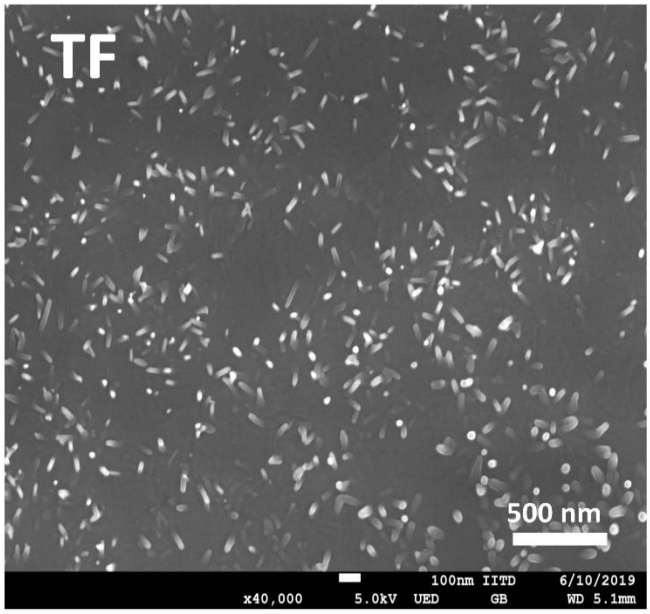

Fig. 4. FESEM image of sample TF showing the growth of vertical nanostructure.

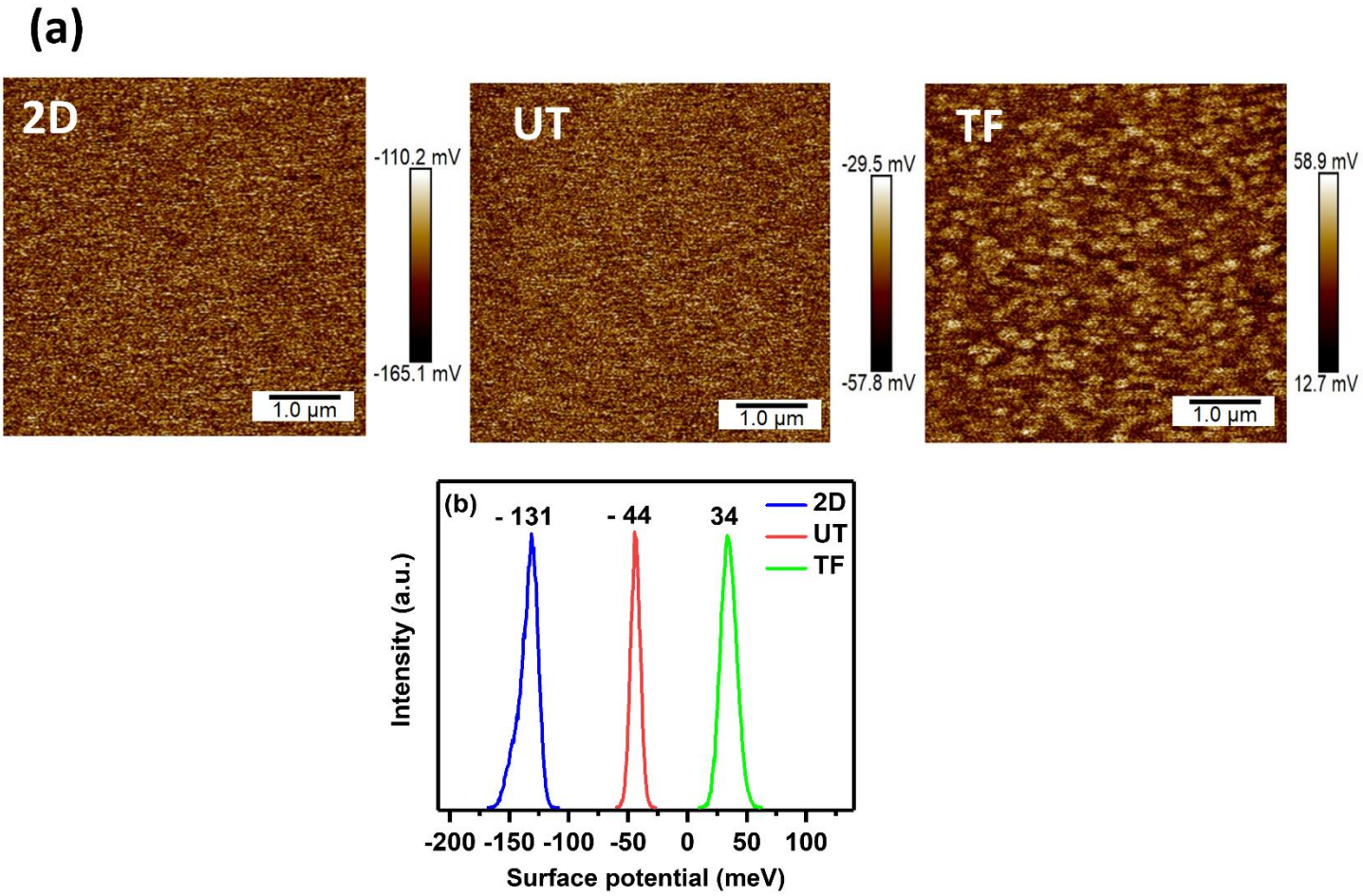

Fig. 5. KPFM investigation of the as-deposited α-MoO_3 films. (a) Microscopic KPFM plots of the sample 2D, UT, and TF show spatial variation of the surface potential (b) Surface potential histograms corresponding to samples 2D, UT, and TF.

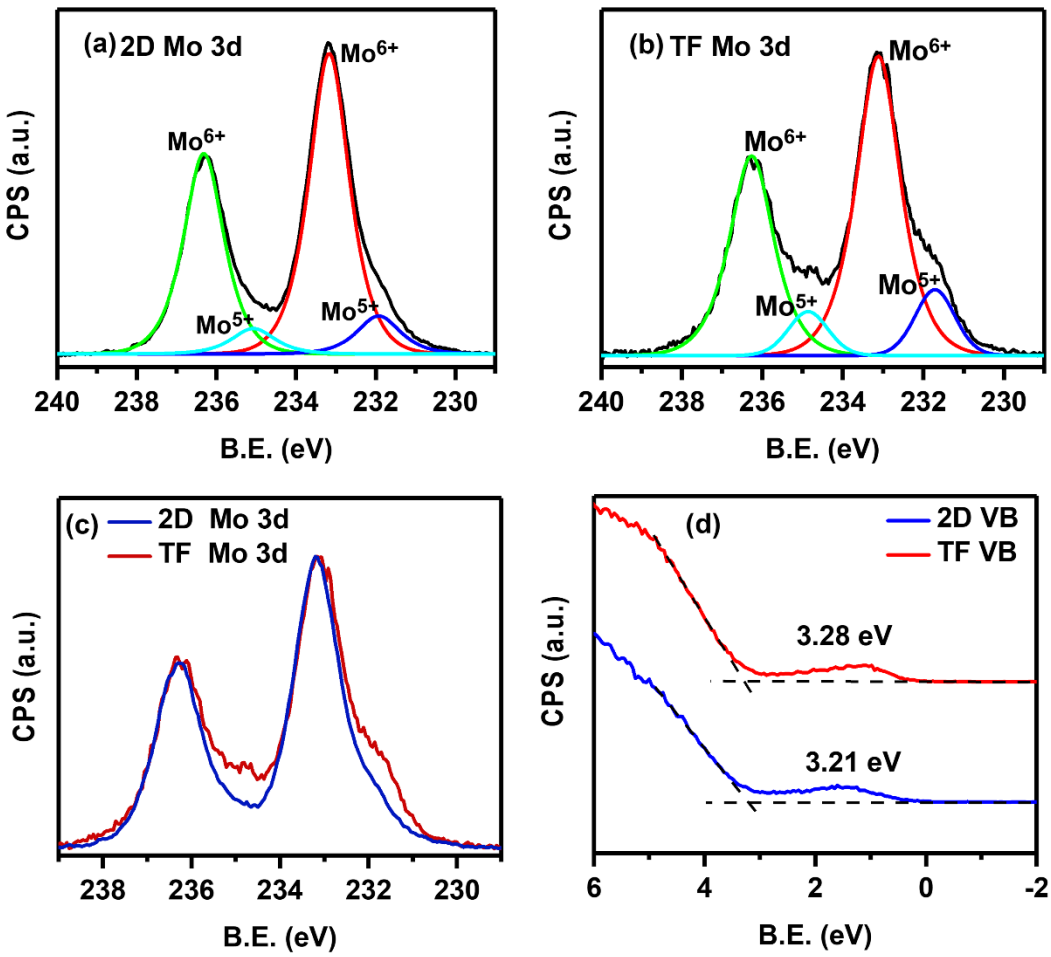

Fig. 6. XPS investigation of sample 2D and TF (a) deconvoluted Mo 3d peaks of sample 2D (b) deconvoluted Mo 3d peaks of sample TF (c) comparison of Mo 3d peaks of sample 2D and TF (d) comparison of the VB maxima spectra of sample 2D and TF.

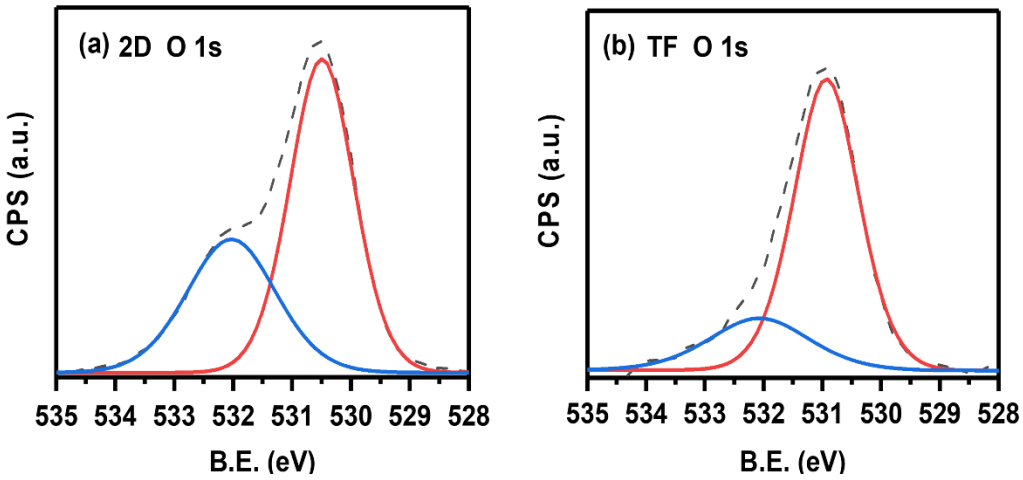

Fig. 7. XPS spectra of the O 1s peak of sample (a) 2D and (b) TF, deconvoluted peak with higher intensity component showing lattice oxygen and the smaller shoulder component represents the adsorbed oxygen species.

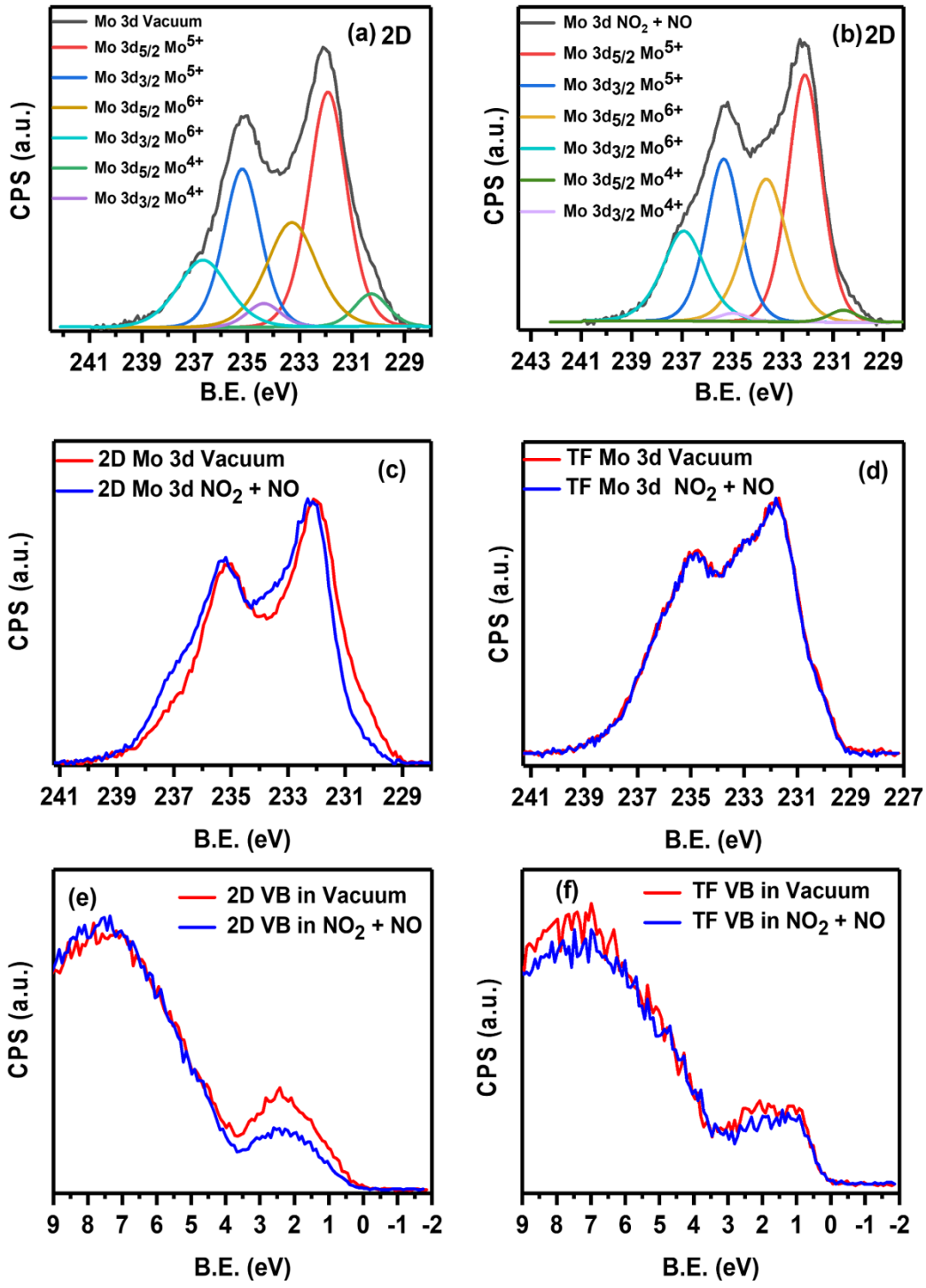
(a) 2D
Mo 3d Vacuum
Mo 3d5/2 Mo5+
Mo 3d3/2 Mo5+
Mo 3d5/2 Mo6+
Mo 3d3/2 Mo6+
Mo 3d5/2 Mo4+
Mo 3d3/2 Mo4+
CPS (a.u.)
241 239 237 235 233 231 229
B.E. (eV)
(b) 2D
Mo 3d NO2 + NO
Mo 3d5/2 Mo5+
Mo 3d3/2 Mo5+
Mo 3d5/2 Mo6+
Mo 3d3/2 Mo6+
Mo 3d5/2 Mo4+
Mo 3d3/2 Mo4+
CPS (a.u.)
243 241 239 237 235 233 231 229
B.E. (eV)
(c)
2D Mo 3d Vacuum
2D Mo 3d NO2 + NO
CPS (a.u.)
241 239 237 235 233 231 229
B.E. (eV)
(d)
TF Mo 3d Vacuum
TF Mo 3d NO2 + NO
CPS (a.u.)
241 239 237 235 233 231 229 227
B.E. (eV)
(e)
2D VB in Vacuum
2D VB in NO2 + NO
CPS (a.u.)
9 8 7 6 5 4 3 2 1 0 -1 -2
B.E. (eV)
(f)
TF VB in Vacuum
TF VB in NO2 + NO
CPS (a.u.)
9 8 7 6 5 4 3 2 1 0 -1 -2
B.E. (eV)

Fig. 8. Ambient pressure XPS investigation of sample 2D and TF (a) deconvoluted Mo 3d peaks of sample 2D in vacuum (b) deconvoluted Mo 3d peaks of sample 2D in NO and NO_2 gas mixture (c) comparison of Mo 3d peaks of sample 2D in vacuum and mixture of NO and NO_2 gas (d) comparison of Mo 3d peaks of sample TF in vacuum and mixture of NO and NO_2 gas. VB maxima spectra of sample (e) 2D and (f) TF in vacuum and mixture of NO and NO_2 gas.

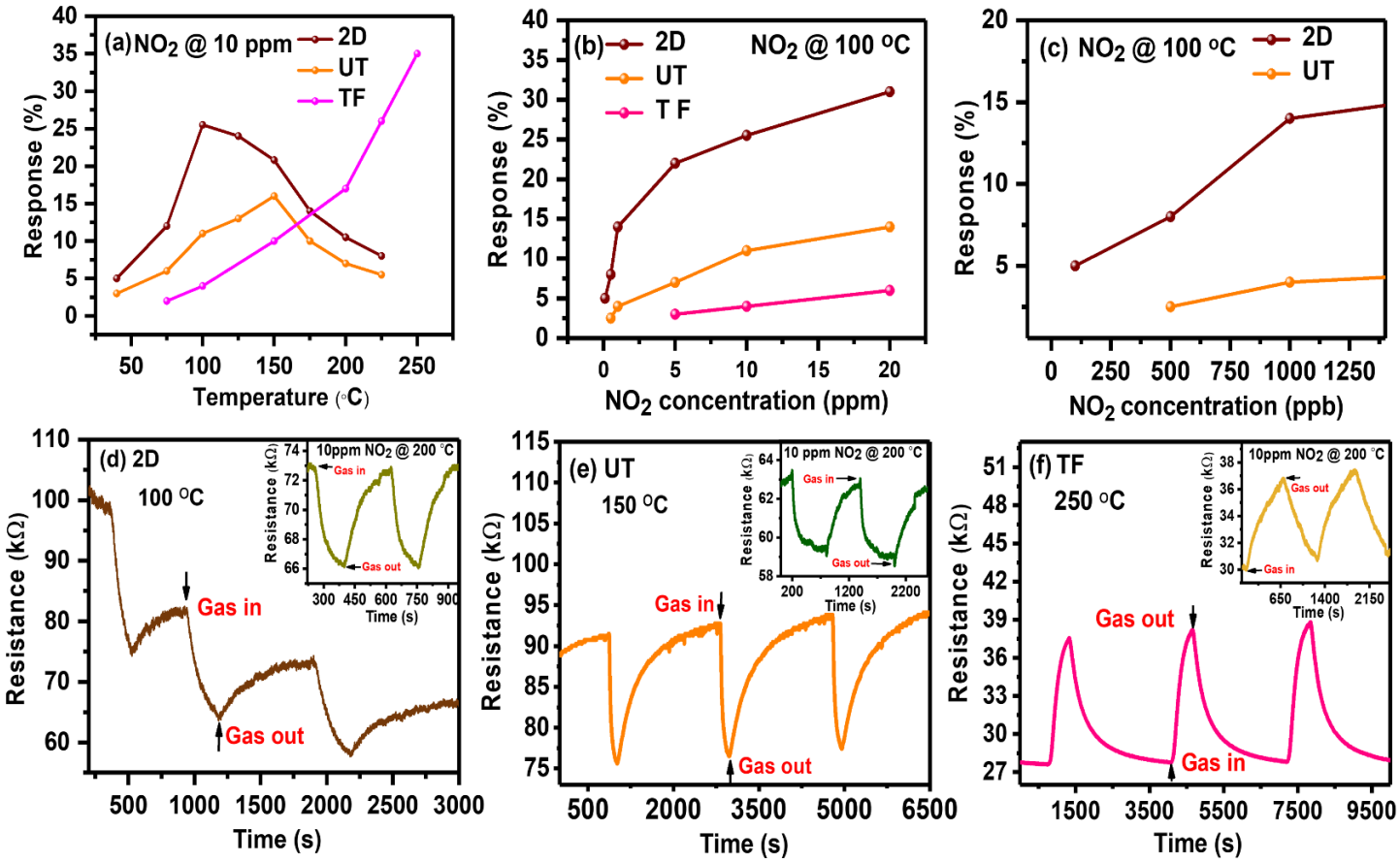

Fig. 9. (a) Comparison of sensing response vs. temperature to obtain optimal working temperature for the sensors (2D, UT, and TF) towards NO_2. (b) and (c) shows a comparison of sensing response vs. NO_2 concentration for sensors (2D, UT, and TF) at an operating temperature of 100 °C. Dynamic response curve show resistance vs. time plot of sample (d) 2D, (e) UT, and (f) TF towards 10 ppm NO_2 at their working temperature. The inset in Figure 9(d)-(f) represents dynamic response curve for sample 2D, UT and TF at 200 °C towards 10 ppm NO_2, respectively.

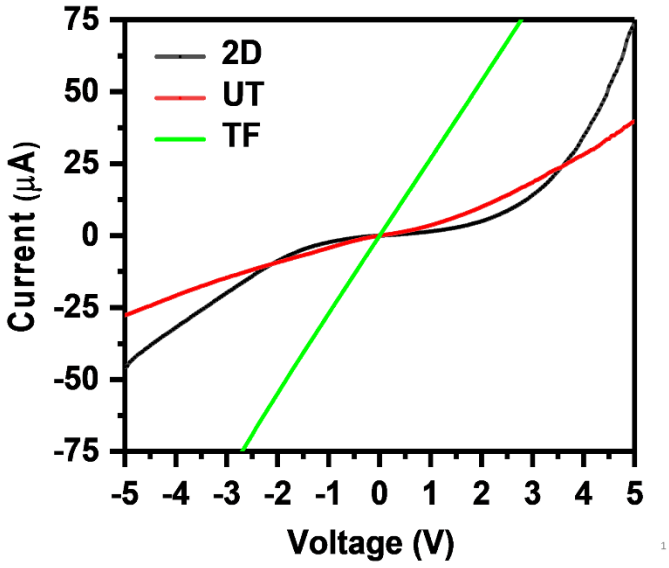

Fig. 10. Comparison of I-V plots of α-MoO_3 sample 2D, UT, and TF at 100 °C.

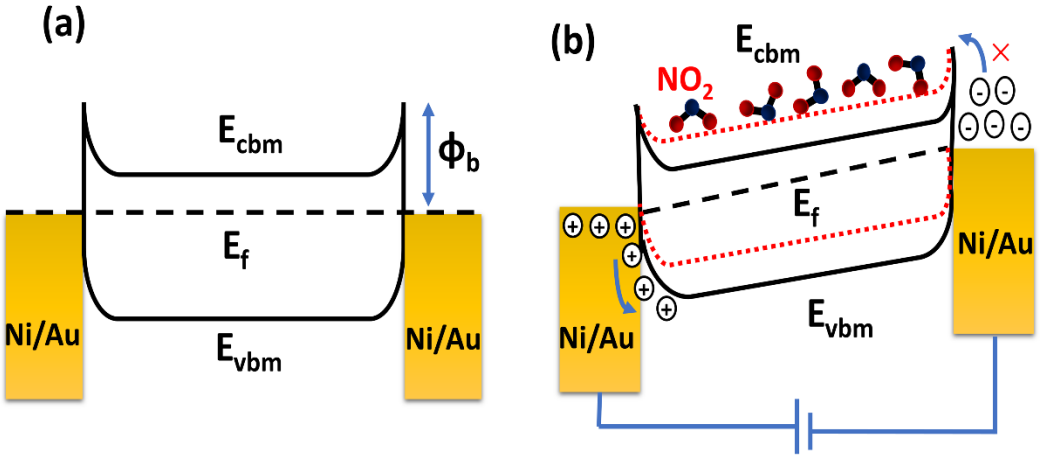

Fig. 11. (a) Energy band diagram of the sample 2D with Ni/Au metal contacts. (b) Energy band diagram under bias in dry air and the presence of NO_2 mixed with dry air.

Table:

Table 1. Comparison of the characteristic deconvoluted Mo 3d peaks from ambient pressure XPS spectra of sample 2D in vacuum and in gas mixture of NO and NO_2

Peak name	Peak position in vacuum (eV)	Peak position in NO and NO_2 (eV)	Peak shift (eV)
Mo $3d_{5/2}$ Mo^{5+}	**231.91**	**232.11**	**0.20**
Mo $3d_{3/2}$ Mo^{5+}	**235.17**	**235.34**	**0.17**
Mo $3d_{5/2}$ Mo^{6+}	**233.29**	**233.65**	**0.36**
Mo $3d_{3/2}$ Mo^{6+}	**236.67**	**236.94**	**0.27**
Mo $3d_{5/2}$ Mo^{4+}	**230.26**	**230.59**	**0.33**
Mo $3d_{3/2}$ Mo^{4+}	**234.36**	**234.95**	**0.59**

Table 2. The response and recovery time for 2D, UT and TF towards 10 ppm NO_2 at 100 °C and 200 °C.

Sample	Operating temperature (°C)	Response (%)	Response time (s)	Recovery time(s)
2D	**100**	**25**	**200**	**-**
	200	**11**	**90**	**136**
UT	**100**	**11**	**424**	**526**
	200	**7**	**267**	**456**
TF	**100**	**4**	**500**	**606**
	200	**17**	**490**	**560**